

Yb- and Er-doped fiber laser Q-switched with an optically uniform, broadband WS₂ saturable absorber

M. Zhang^{1,*,+}, G. Hu^{2,+}, G. Hu¹, R. C. T. Howe², L. Chen^{3,*}, Z. Zheng^{1,4}, and T. Hasan²

¹School of Electronic and Information Engineering, Beihang University, Beijing, 100191, China

²Cambridge Graphene Centre, University of Cambridge, Cambridge, CB3 0FA, UK

³Shenzhen Key Laboratory of Laser Engineering, College of Optoelectronics Engineering, Shenzhen University, Shenzhen, 518060, China

⁴Collaborative Innovation Center of Geospatial Technology, Wuhan, 430079, China

*mengzhang10@buaa.edu.cn

*l.chen10@szu.edu.cn

+these authors contributed equally to this work

ABSTRACT

We demonstrate a ytterbium (Yb) and an erbium (Er)-doped fiber laser Q-switched by a solution processed, optically uniform, few-layer tungsten disulfide saturable absorber (WS₂-SA). Nonlinear optical absorption of the WS₂-SA in the sub-bandgap region, attributed to the edge-induced states, is characterized by 3.1% and 4.9% modulation depths with 1.38 and 3.83 MW/cm² saturation intensities at 1030 and 1558 nm, respectively. By integrating the optically uniform WS₂-SA in the Yb- and Er-doped laser cavities, we obtain self-starting Q-switched pulses with microsecond duration and kilohertz repetition rates at 1030 and 1558 nm. Our work demonstrates broadband sub-bandgap saturable absorption of a single, solution processed WS₂-SA, providing new potential efficacy for WS₂ in ultrafast photonic applications.

Introduction

Two dimensional (2d) nanomaterials such as mono- or few-layer graphene, semiconducting transition metal dichalcogenides (s-TMDs) and black phosphorous exhibit high third-order optical nonlinear susceptibility and ultrafast carrier dynamics, making them attractive for nonlinear photonics and optoelectronics.¹⁻³ Amongst the 2d materials, s-TMDs are of particular research interest due to their diversity and the distinct yet complementary properties to graphene they offer. TMDs, a family of ~40 different layered materials, have a general formula MX₂, where M is a transition metal atom (e.g. Mo, W or Nb) and X is a chalcogen atom (a group of VI element, e.g. S, Se or Te). Each TMD layer consists of a single plane of M atoms held between two planes of X atoms by strong covalent bonds. Depending on the coordination and oxidation states of the M atoms, TMDs may behave as metallic, semiconducting or insulating. Similar to other layered materials (LMs), the individual layers in TMD bulk crystals are stacked together by relatively weak van der Waals forces, allowing their exfoliation into single and few layer forms. The optoelectronic properties of s-TMDs are strongly thickness-dependent. For example, the bandgap of s-TMDs typically shifts from indirect for bulk material to direct for monolayer flakes.^{1,4} Collectively, the bandgaps of s-TMDs span the visible and near-infrared spectrum.¹ Such layer-dependent characteristics make s-TMDs comparable or even superior to the zero-gap graphene for a variety of (opto)electronic and photonic applications.¹ s-TMDs also offer the possibility of engineering their optical properties for desirable performances.⁵ We note that while black phosphorous has recently attracted a strong interest,^{3,6,7} poor material stability, even for over a few days, remains a significant drawback.³

s-TMDs have been shown to possess remarkable optical and optoelectronic properties, including high optical nonlinear susceptibility,^{8,9} ultrafast carrier dynamics¹⁰ and broadband working wavelength range,^{11,12} in addition to robustness and environmental stability. This has led to the demonstration of numerous nonlinear optical phenomena using s-TMDs, including saturable absorption^{11,12} (i.e. reduced optical absorption with increased intensity of incident light¹³) and optical parametric processes (i.e. second^{8,14} and third⁹ harmonic generation), suggesting that these materials could be a suitable platform for the development of photonic devices. One such potential application exploiting the saturable absorption property is in the generation of short pulses by mode-locking or Q-switching in laser cavities, where saturable absorber (SA) devices act as a passive optical switch to modulate the intra-cavity loss.¹³ Such short-pulsed or ‘ultrafast’ lasers have become an indispensable tool, playing an increasingly important role in a wide range of applications, including biomedical imaging and therapy, materials processing, fundamental research and military.¹⁵ Unlike graphene, which has a linear dispersion of Dirac electrons enabling

broadband saturable absorption, s-TMDs typically have a (bulk and monolayer) bandgap ranging between $\sim 1\text{--}2\text{ eV}$.¹ Some recent progresses have been made in measuring the saturable absorption of s-TMDs in the visible region,^{16,17} suggesting their potential as a SA device to produce short pulses in this spectral range.

Similar nonlinear optical absorption and fast carrier dynamics in s-TMDs have also been reported in the near-infrared region.^{11,18–20} In particular, a number of studies have reported the generation of short pulses from fiber lasers operating at ~ 1.0 ,^{18–20} 1.55 ^{11,18,20} and $1.9\text{ }\mu\text{m}$ ^{18,20} using several sulfide and selenide-based s-TMDs, including molybdenum disulfide (MoS_2) and molybdenum diselenide (MoSe_2). More recently, tungsten disulfide (WS_2) has also been demonstrated to achieve mode-locking and Q-switching, but only in Er-doped fiber lasers.^{21–25} While the operating wavelengths of these lasers correspond to photon energies below either the bulk or monolayer bandgap of these s-TMDs, the processes behind this sub-bandgap absorption are yet to be fully understood. Therefore, it is of significant importance to investigate the governing physical mechanism of saturable absorption of WS_2 in the near-infrared region and its applicability as a wideband SA material.

Mono- or few-layer WS_2 can be produced through a variety of methods, with mechanical cleavage, chemical vapor deposition (CVD) and solution processing techniques such as ultrasonic assisted liquid phase exfoliation (UALPE) being the most commonly exploited ones. In particular, UALPE allows mass production of chemically pristine mono- and few-layer WS_2 flakes under ambient conditions, without the need for high temperature and complex transfer procedures associated with CVD. As with the other LMs, WS_2 dispersions produced via UALPE can be printed onto optical components such as quartz substrates, mirrors and fiber facets or blended with polymers to form composites for simple integration into a laser cavity, making this strategy very attractive for a wide range photonic and optoelectronic applications.^{12,15,26}

Here, we fabricate a few-layer WS_2 polymer composite SA based on UALPE for short pulse generation. The free-standing SA exhibits high spatial uniformity in nonlinear optical properties. The modulation depth of the WS_2 -SA is 3.1% at 1030 nm and 4.9% at 1558 nm, respectively. Using a single WS_2 -SA composite, we demonstrate microsecond-duration Q-switched pulses with kilohertz repetition rates in all-fiber Yb- and Er-doped lasers to underscore its applicability as a broadband SA material.

Results

Sample preparation and characterization

We fabricate the SA as a freestanding polymer composite film using WS_2 nanoflakes produced by UALPE of bulk WS_2 crystals. The UALPE process for WS_2 is similar to that used for other LMs such as graphene^{27,28} and several other TMDs,^{11,12,29–31} consisting of two steps. First, bulk crystals of WS_2 are mixed with a suitable solvent and exfoliated via mild ultrasonication. This relies on the formation of microbubbles in the solvent resulting from the high-frequency (usually $\sim 20\text{--}60\text{ kHz}$) pressure variations.³² Under appropriate frequency, pressure and solvent conditions, these microbubbles become unstable as they grow in size and eventually collapse.³² The shockwaves produced from the collapsed microbubbles create strong shear forces that are sufficient to overcome the weak van der Waals forces between the layers in bulk LM crystals, resulting in exfoliation of thinner flakes. The second step involves removal of the unexfoliated, thicker flakes. This is typically achieved via centrifugation or filtration.^{28,33} Thus, UALPE and subsequent processing of WS_2 bulk crystals produce exfoliated mono-, bi- and few-layer WS_2 flakes in suitable solvents.

The stability of the exfoliated WS_2 (and other LMs) dispersion is dependent on minimizing the enthalpy of mixing ΔH .^{33,34} It has been demonstrated that ‘good’ solvents for exfoliation have dispersive (δ_D), polar (δ_P) and hydrogen bonding (δ_H) Hansen solubility parameters³⁵ that match those empirically derived for WS_2 ($\delta_D \sim 18\text{ MPa}^{1/2}$, $\delta_P \sim 8\text{ MPa}^{1/2}$, $\delta_H \sim 7.5\text{ MPa}^{1/2}$).³⁶ However, the best-suited solvents (e.g. N-cyclohexyl-2-pyrrolidone [CHP], cyclohexanone and N-methyl-2-pyrrolidone [NMP]) are challenging for device/composite processing due to their relatively high boiling points (NMP $\sim 202^\circ\text{C}$, cyclohexanone $\sim 155^\circ\text{C}$, CHP $\sim 154^\circ\text{C}$). UALPE in pure lower boiling point solvents such as alcohols and water does not typically yield stable dispersions due to relatively strong mismatch between δ_D , δ_P and δ_H of these solvents to those of WS_2 . In this case, surfactants can be used to stabilize the dispersion. Such stable dispersions are necessary for the fabrication of optically homogeneous composite SAs, as the slow drying process would otherwise allow aggregates to form,¹⁵ leading to scattering losses and unreliable device performance.^{15,37} This approach has therefore been widely used to fabricate 1d and 2d material-based SAs.^{20,26–28,38}

It has been experimentally shown with graphene that quasi-2d surfactants with hydrophobic and hydrophilic faces (e.g. sodium deoxycholate [SDC], a bile salt surfactant) are well-suited to exfoliating and stabilizing hydrophobic 2d materials (such as WS_2) in water.²⁸ For stable dispersions, the surfactant should be present at a concentration in excess of the temperature dependent critical micelle concentration (CMC), defined as the surfactant concentration above which its molecules can spontaneously self-arrange to form micelles in water.³⁹ Therefore, if exfoliated hydrophobic flakes (such as WS_2) are present in a water-surfactant solution above the corresponding CMC value, the surfactant molecules are expected to encapsulate and stabilize the flakes, preventing their reaggregation and sedimentation.^{28,34,40,41}

We prepare the stable few-layer WS_2 dispersion by mixing 100 mg WS_2 crystals with $\sim 70\text{ mg}$ SDC surfactant in 10 mL of DI water and sonicating for 12 hours in a bath sonicator at $\sim 15^\circ\text{C}$. We select SDC, a di-hydroxy bile salt surfactant over the

more commonly used sodium cholate (SC), a tri-hydroxy bile salt due to its higher hydrophobic index, which should allow stronger interaction between the surfactant and WS₂.²⁸ The CMC of SDC in water at room temperature is found to be 4.7 mM ($\sim 2 \text{ g.L}^{-1}$) by pendant droplet measurement of the surface tension of different concentration SDC solutions (the surface tension of solutions changes rapidly below the CMC, but stabilizes above). Thus the surfactant concentration we use here is ~ 3.5 times the CMC, sufficient to adequately support the exfoliated WS₂.^{28,42,43} The sonicated dispersion, containing a mixture of exfoliated and unexfoliated materials, is centrifuged at $\sim 1500 \text{ g}$ for one hour. The top 70% of the dispersion, enriched with mono-, bi- and few layer flakes, is then decanted for characterization and SA fabrication.

Dispersion characterization

The optical absorption spectrum of the WS₂ dispersion, diluted to 10% v/v to reduce scattering effects,⁴⁴ is shown in Fig. 1(a), with the inset of a photograph of the cuvette containing the dispersion. The spectrum shows the characteristic WS₂ excitonic peaks, referred to as A (at $\sim 630 \text{ nm}$) and B (at $\sim 520 \text{ nm}$) according to common nomenclature.⁴⁵ The spectrum can be used to estimate the concentration of WS₂ using Beer-Lambert law ($A_\lambda = \alpha_\lambda c l$), where c is the WS₂ concentration (g.L^{-1}), l is the distance the light passes through the dispersion (m) and A_λ and α_λ are the absorption (a.u.) and material dependent optical absorption coefficient ($\text{L.g}^{-1}\text{m}^{-1}$) at wavelength λ (nm), respectively. Using a combination of optical absorption spectroscopy and thermogravimetric analysis on a set of dispersions,¹¹ we estimate the value of α_{630} for WS₂ $\sim 1324 \text{ L.g}^{-1}\text{m}^{-1}$. From this, we estimate the concentration of dispersed WS₂ to be 0.23 g.L^{-1} .

The distribution of flake thicknesses and lateral dimensions is measured via atomic force microscopy (AFM). Samples are prepared by drop-casting a diluted (5% v/v) WS₂ dispersion onto a Si/SiO₂ wafer. The wafers are then rinsed with DI water to remove residual surfactant, giving clean and isolated flakes on the substrates. A typical flake is shown in Fig. 1(b). The corresponding height profile, presented in Fig. 1(c), shows a thickness of $\sim 5 \text{ nm}$. The average thickness [Fig. 1(d)], measured across ~ 400 individual flakes, is $(5.0 \pm 0.1) \text{ nm}$. We find $\sim 73\%$ of the flakes are $\leq 5 \text{ nm}$ thick, corresponding to < 8 layers, assuming $\sim 1 \text{ nm}$ for a monolayer flake and 0.6 nm for each subsequent layer.⁴⁶ As shown in Fig. 1(e), the average lateral dimension of the flakes is $(62 \pm 1) \text{ nm}$.

Composite characterization

To allow integration of the SA into the fiber laser cavity, a free-standing composite film is prepared from the WS₂ dispersion using an approach previously demonstrated for other 1d and 2d materials.^{11,12,15,20,26–29,38} The composite is prepared by homogeneously mixing the WS₂ dispersion with a 5 wt% aqueous solution of polyvinyl alcohol (PVA) polymer. PVA is used as the host polymer because it does not exhibit strong optical absorption at 1030 and 1558 nm, its solvent compatibility (PVA is water soluble), ease of processability (can be processed at room temperature), robustness and flexibility (dried thin films have high tensile strength and are not brittle). The mixture is poured into a Petri dish and allowed to dry at room temperature in a desiccator, producing a $\sim 30 \mu\text{m}$ thick, free-standing WS₂-polymer composite SA [Fig. 2(a) inset].

For transmissive type thin film SA devices, optical uniformity without defects (such as cracks, voids, material aggregates etc.) is an important consideration to ensure reliable and repeatable device performance. The uniformity and quality of the WS₂-SA is assessed by using optical microscopy, a commonly used technique employed for other nanomaterial based SAs.^{15,20} The optical micrograph, shown in Fig. 2(a), confirms the absence of $> 1 \mu\text{m}$ aggregates in the SA composite, which would otherwise have led to undesirable nonsaturable scattering losses.⁴⁴

Figure 2(b) shows the optical absorption of the composite film. Measurement of a pure PVA film prepared by the same method is also included in Fig. 2(b) as a reference. We note that the WS₂-SA composite shows non-zero absorption, even at energies below bandgap of either bulk ($\sim 1.3\text{--}1.4 \text{ eV}$, $954\text{--}886 \text{ nm}$ ^{1,47,48}) or monolayer ($\sim 2.1 \text{ eV}$, 590 nm ^{1,48}) WS₂. Considering contributions from PVA (0.011–0.015 absorbance, 2.5–3.4%) [Fig. 2(b)] the WS₂-PVA composite shows a marked increase in absorption (0.046–0.039 absorbance, 10.05%–8.6%), indicating strong optical absorption from the embedded WS₂ flakes at both 1030 (1.2 eV) and 1558 nm. We have recently attributed this sub-bandgap light absorption in other s-TMD materials (MoS₂,^{11,12,49} MoSe₂²⁰) to edge-induced sub-bandgap states.^{11,12,20,29} We propose that similar edge-induced states arise within the material bandgap in our UALPE WS₂ flakes, leading to the observed sub-bandgap light absorption.

The nonlinear optical absorption of the WS₂-SA is characterized using an open-aperture Z-scan technique. For this, an ultrashort fiber source operating at 1030 nm is used as the pump light (120 fs pulse duration, 20 MHz pulse repetition rate), split using a 90%:10% fused fiber coupler, the latter enabling monitoring of power used as a reference. The SA composite is swept through the focus of a beam of the remaining port and the transmitted power is recorded as a function of incident intensity on the device. A typical dataset from a single Z-scan measurement, at a fixed transverse position on the WS₂-SA, shown in Fig. 3(a), can be well-fitted with the two-level SA model.⁵⁰ From the fit, the following SA parameters are extracted: at 1030 nm, the saturation intensity, $I_{\text{sat},1030} \sim 1.38 \text{ MW/cm}^2$, modulation depth, $\alpha_{s,1030} \sim 3.1\%$ and nonsaturable absorption, $\alpha_{ns,1030} \sim 6.9\%$. The same measurement is also carried out at the wavelength of 1558 nm (150 fs pulse duration, 10 MHz pulse repetition rate). The measured parameters are: $I_{\text{sat},1558} 3.83 \text{ MW/cm}^2$, $\alpha_{s,1558} \sim 4.9\%$, and $\alpha_{ns,1558} \sim 3.7\%$, respectively [Fig 3(d)]. Thus, the WS₂-SA shows strong saturable absorption in both these wavelengths.

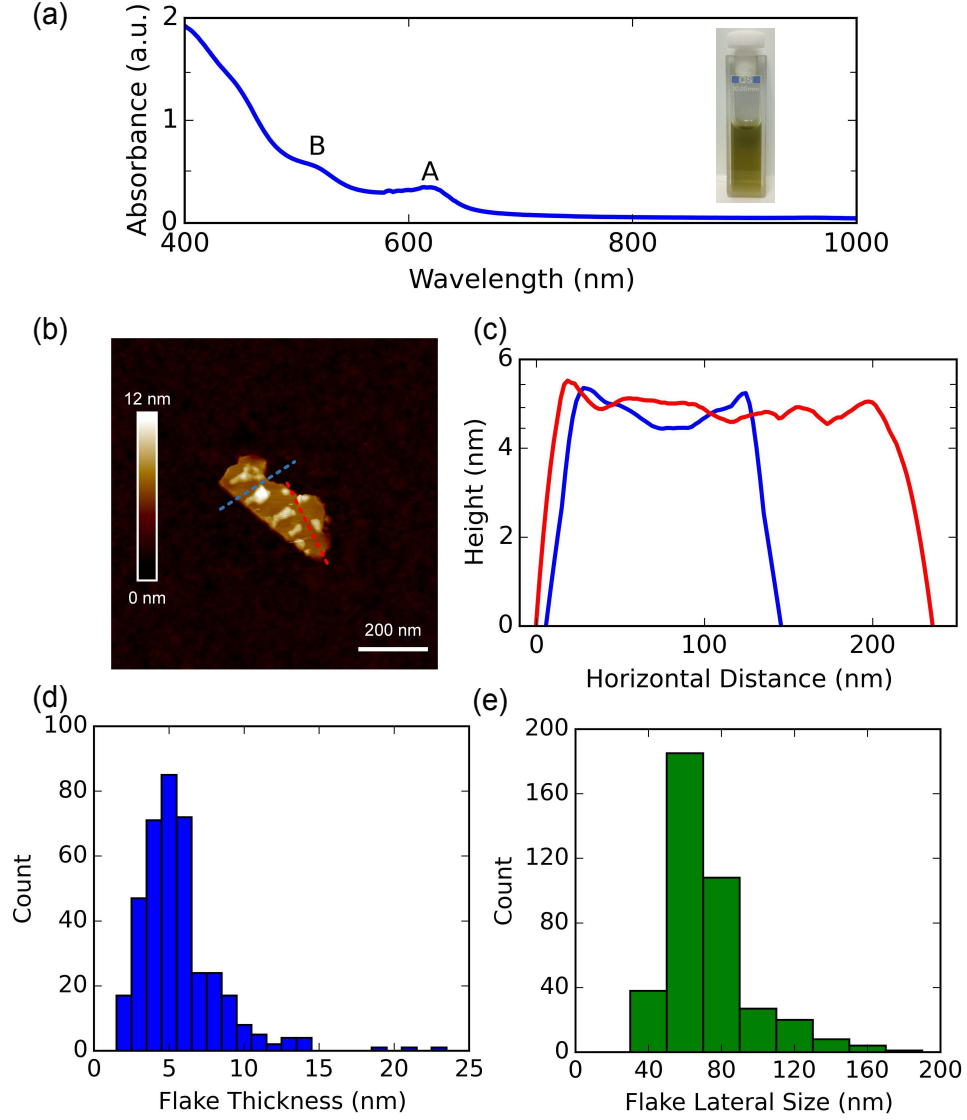


Figure 1. (a) Linear optical absorption of WS₂ flakes in a 10% v/v dispersion. Inset, Stable WS₂ dispersion (diluted to 10% v/v) in a cuvette; (b) AFM image of a typical WS₂ flake; (c) height variations of the flakes along the marked line; (d) TEM distribution of flake thickness; (e) distribution of lateral WS₂ flake dimensions.

The uniformity of the WS₂ flakes embedded in the free-standing WS₂-PVA composite is next evaluated by raster scanning the sample. This is essential to ensure reliable and repeatable performances of the WS₂-SA devices. For this, we measure the nonlinear saturation of the $\sim 30 \mu\text{m}$ SA with 0.5 mm spatial increments in the XY plane, across a 2×2 mm section, at both wavelengths. The extracted data, processed to display the variation in $\alpha_{s,1030}$ and $\alpha_{s,1558}$ [Fig. 3(b) and (e)] and $I_{sat,1030}$, $I_{sat,1558}$ [Fig. 3(c) and (f)] are presented on two-dimensional grids. The spatial increment, i.e. the resolution in the scanning, is limited by the laser spot size during the measurement. Figure 3(b), (c), (e), (f) show clear evidence of optical homogeneity (with standard deviations of 0.13%, 0.17 MW/cm², 0.13%, 0.11 MW/cm², respectively), allowing us to obtain repeatable performance across the WS₂-SA sample.

Demonstration of Q-switching a fiber laser using few-layer WS₂-SA

The demonstrated sub-bandgap saturable absorption of the few-layer WS₂-PVA composite at 1030 and 1558 nm indicates that the device could be used to modulate the loss and Q-factor of a fiber laser cavity. This could in turn be exploited to generate a regular train of Q-switched pulses in this spectral region. To explore the potential of using a single WS₂-SA for short-pulse generation at different wavelengths, fully fiber-integrated Yb- and Er-doped lasers are constructed. For each laser cavity, a

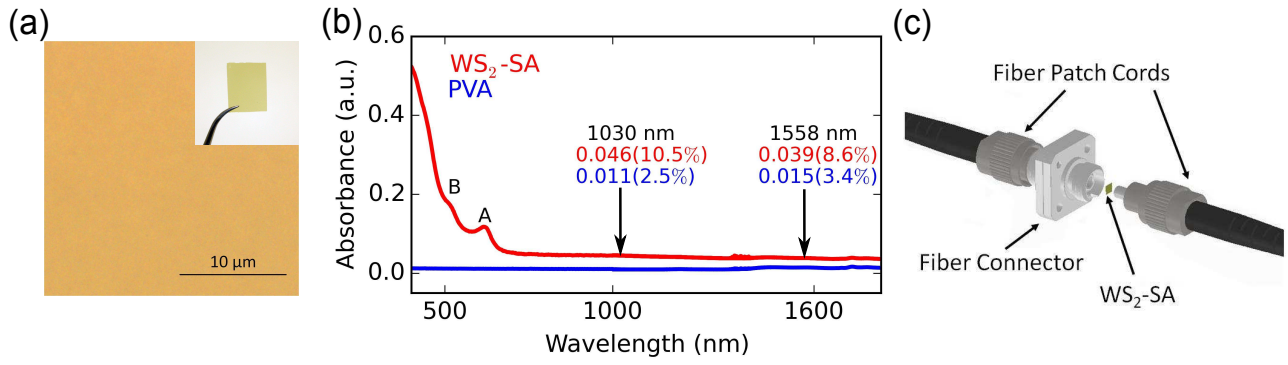


Figure 2. (a) Optical micrograph of the free-standing WS_2 -PVA SA composite, confirming absence of aggregates. Inset, photograph of WS_2 -SA. (b) Optical absorbance of a pure PVA and WS_2 -PVA SA. (c) Schematic showing integration of WS_2 -PVA SA device between two fiber patch cords.

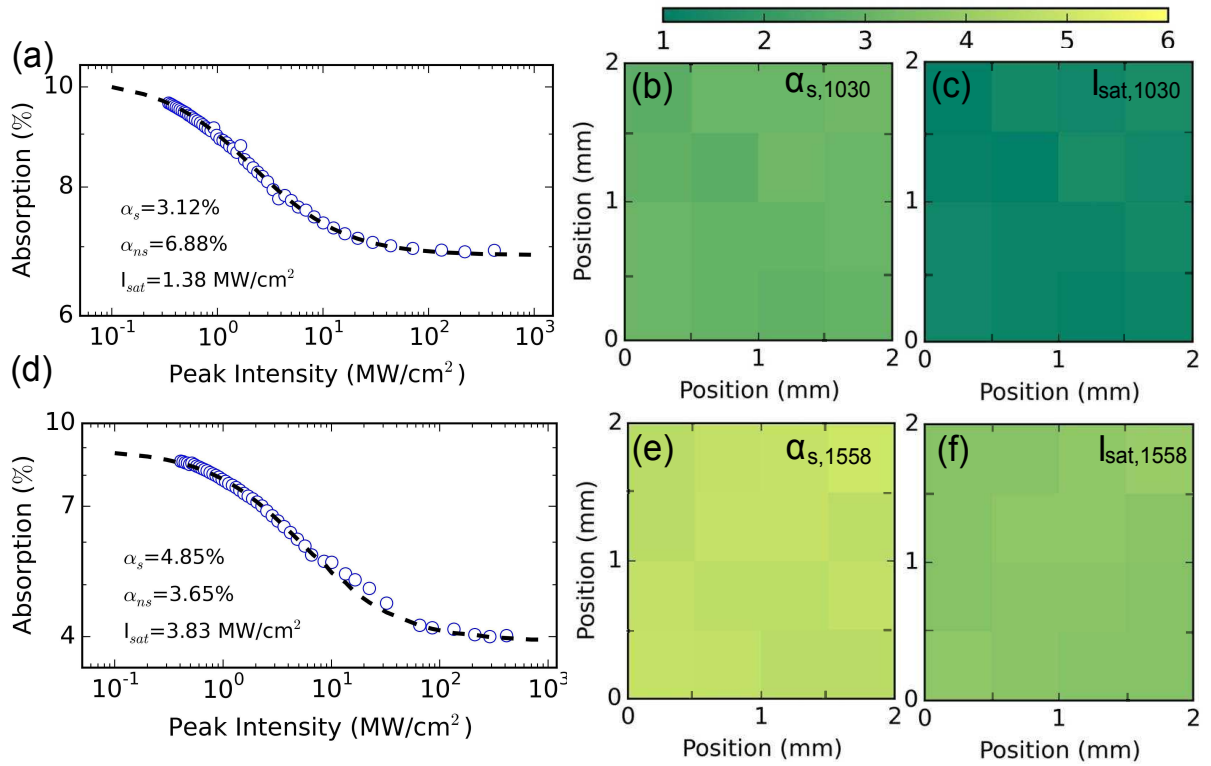


Figure 3. Nonlinear optical absorption at (a)-(c) 1030 nm and (d)-(f) 1558 nm measured by an open aperture Z-scan technique. (a), (d) Typical datasets from Z-scan experiment. Mapping of the homogeneity of the sample used in the experiment: variation in modulation depth (b), (e), colorbar: 1 – 6%; and saturation intensity (c), (f), colorbar: 1 – 6 MW/cm^2 .

ring configuration is adopted, consisting of entirely isotropic, single-mode fiber. The Yb and Er fiber amplifiers consist of single-mode Yb- and Er-doped active fiber, respectively, co-pumped by a 974 nm pump diode. In addition to the fiber amplifier, each cavity includes a polarization-independent optical isolator to ensure unidirectional propagation, fused-fiber output coupler for both spectral and temporal diagnostics and polarization controller to adjust the net cavity birefringence [Fig. 4(a) and 5(a)]. The WS_2 -SA is integrated into the cavities by sandwiching a $\sim 1 \text{ mm} \times 1 \text{ mm}$ of the composite between two fiber patch chords, shown in Fig. 2(c). The total cavity length for the Yb- and Er-doped lasers is 66 m and 9 m, respectively.

Q-switched Yb-doped fiber laser characterization

Self-starting Q-switching is obtained from the all-fiber integrated Yb-doped laser, generating a stable train of pulses, centered at 1030 nm [Fig. 4(e)]. Typical output characteristics of the laser, at 0.5 mW average output power, are shown in Fig. 4. Pulses are generated with 27.2 μ s spacing, corresponding to 36.7 kHz repetition rate [Fig. 4(b)] and a full width at half maximum (FWHM) pulse duration of 3.2 μ s [Fig. 4(c)]. The radio frequency (RF) spectrum of the output shows a high signal-to-background contrast of 45 dB [Fig. 4(d)], indicating good pulse train stability, comparable to Q-switched fiber lasers based on other 2d layered materials.^{12,51,52}

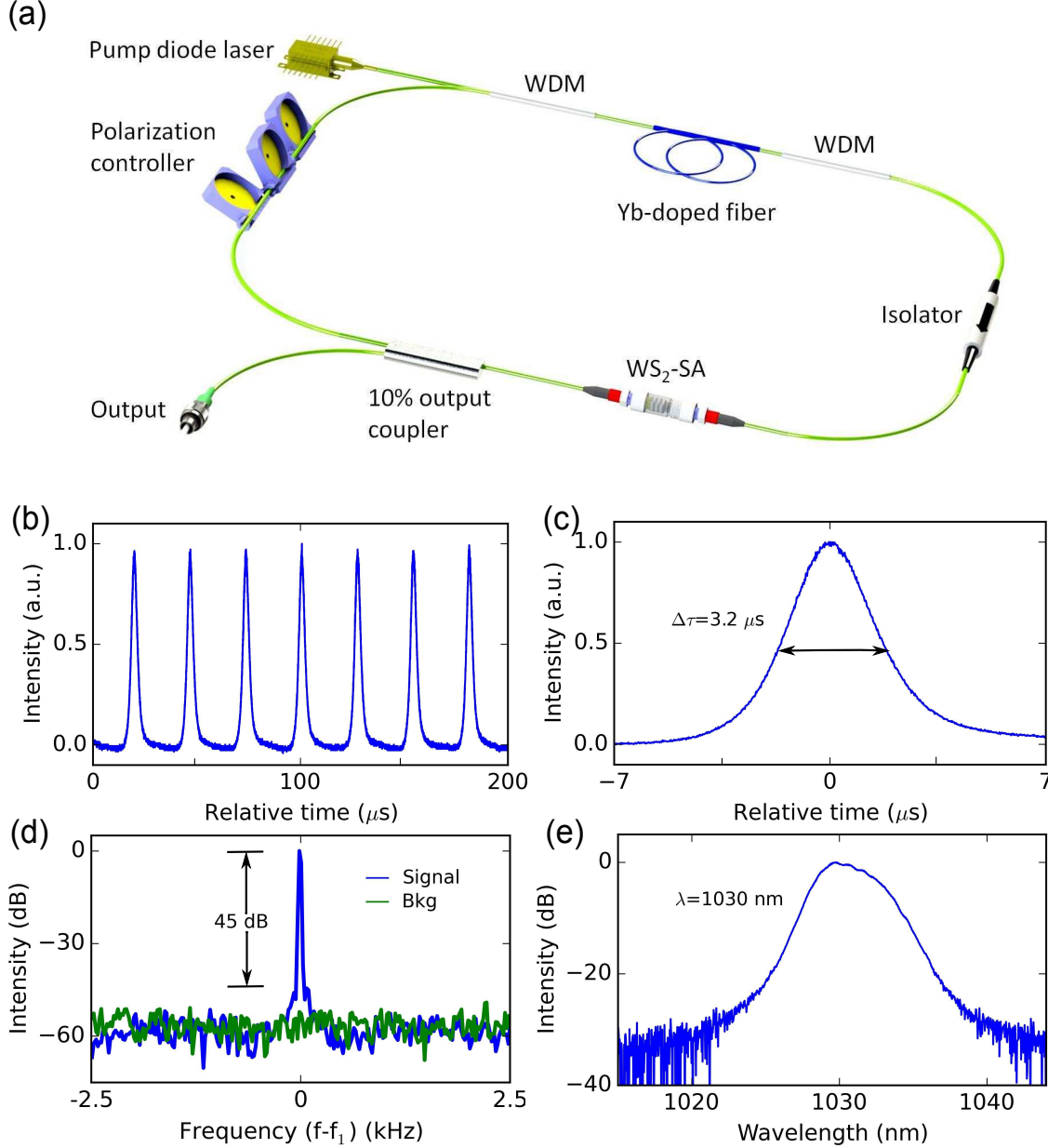


Figure 4. Q-switched Yb-doped fiber laser: (a) cavity configuration; (b) output pulse train, with a spacing of 27.2 μ s; (c) single pulse profile, with 3.2 μ s FWHM pulse width; (d) radio frequency spectrum of fundamental frequency on a 5 kHz span, where $f_1 = 36.7$ kHz, with the green trace showing the noise floor of the RF analyzer; (e) measured optical spectrum.

The pulse properties in continuous-wave pumped Q-switched lasers rely on nonlinear dynamics in the gain medium and SA. This leads to a dependence of cavity repetition rate and pulse duration on pump power.⁵³ A pulse is emitted once the storage energy of the cavity reaches a certain threshold. Therefore, a greater pump power enables higher repetition rates and results in shorter pulses. This is experimentally observed by changing the pump power as the pulse duration is reduced from 6.4 μ s to 3.2

μs and the cavity repetition rate is increased from 24.9 kHz to 36.7 kHz [Fig. 6(a)]. The maximum pulse energy is 13.6 nJ, limited by the available pump power. We believe that higher pulse energies could be achieved by further optimizing the laser cavity. The pulse duration could also be further shortened by reducing the length of the laser cavity.

Q-switched Er-doped fiber laser characterization

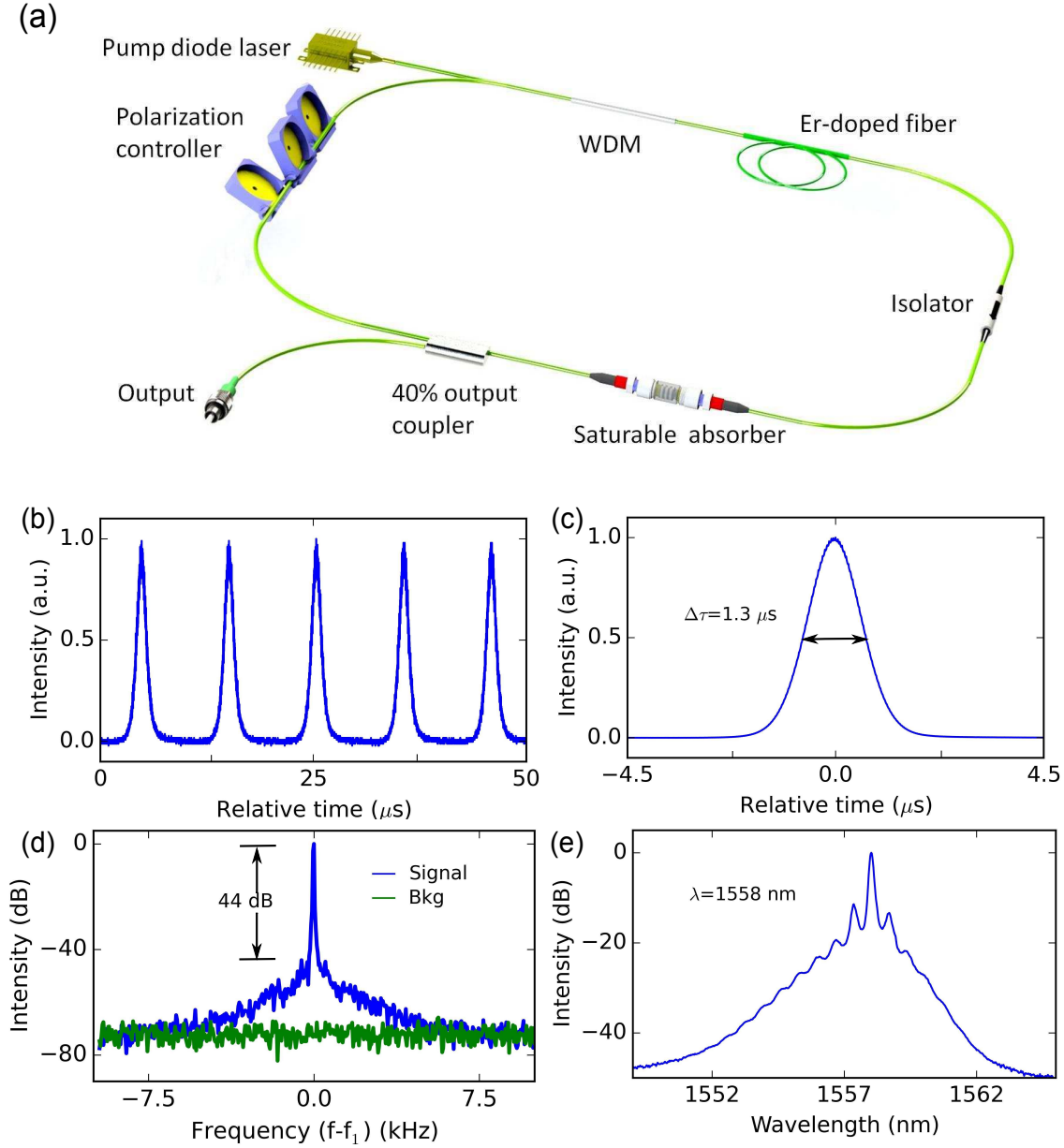


Figure 5. Q-switched Er-doped fiber laser: (a) cavity configuration; (b) output pulse train, with a spacing of 10.3 μs ; (c) single pulse profile, with 1.3 μs FWHM pulse width; (d) radio frequency spectrum of fundamental frequency on a 20 kHz span, where $f_1 = 97\text{kHz}$, with the green trace showing the noise floor of the RF analyzer; (e) measured optical spectrum.

To demonstrate the sub-bandgap saturable absorption for short pulse generation at a longer wavelength, the same SA is subsequently incorporated into the Er-doped fiber laser described above. Self-starting Q-switching operation is achieved at 1558 nm [Fig. 5(e)] with an average output power of 6.4 mW. Typical output pulse train properties are shown in Fig. 5(b). The cavity repetition rate is 97.1 kHz, corresponding to a pulse-to-pulse spacing of 10.3 μs . Figure 5(c) shows the single pulse profile, with a FWHM pulse duration of 1.3 μs . The signal-to-noise background contrast of RF spectrum, plotted in Fig. 5(d) is 44 dB, again, showing the good pulse train stability of the Er-laser. With increasing pump power, the repetition rate is tuned

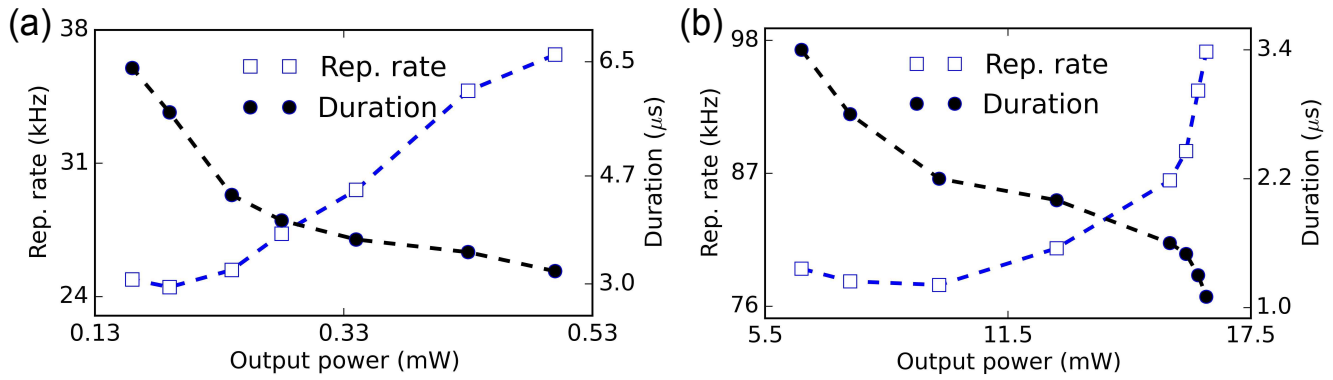


Figure 6. Variation of the pulse duration and repetition rate with average output power for Q-switched (a) Yb-, (b) Er-doped fiber lasers using few-layer WS₂-PVA composite SA.

from 79 kHz to 97 kHz, with corresponding pulse duration from 3.4 μ s to 1.1 μ s as the average output power is increased from 6.4 mW to 16.4 mW [Fig. 6(b)]. The pulse energy is 179.6 nJ at the highest output power.

Discussion

Following stable Q-switching results obtained by using the WS₂-SA composite at 1030 and 1558 nm, the same experiment is conducted with a ~ 30 μ m-thick pure PVA film (fabrication process similar to that used for WS₂-SA fabrication, but without the WS₂ flakes). No Q-switching is observed at any power level or polarization controller position, confirming that the sub-bandgap saturable absorption arises from the few-layer WS₂ flakes.

As discussed before, the WS₂-SA exhibits non-zero sub-bandgap absorption at energies below the bulk (~ 1.3 - 1.4 eV, 954-886 nm^{1,47,48}) or monolayer (~ 2.1 eV, 590 nm^{1,48}) WS₂ bandgap. The sub-bandgap absorption and its nonlinear behavior is also verified by Z-scan measurement and demonstration of Q-switched lasers at 1030 (1.2 eV) and 1558 nm (0.8 eV). Similar observation of sub-bandgap saturable absorption in other s-TMDs have also been reported.^{11,18–20} For the case of MoS₂ and MoSe₂, we recently proposed that the sub-bandgap absorption arises from edge-induced sub-bandgap states.^{11,12,20} Our proposal is based on previous experimental observations of increased sub-bandgap absorption in lithographically patterned MoS₂ compared to their large crystals due to increased edge to surface area ratio.⁴⁹ From the AFM data and considering approximately square flakes for ease of calculation, we estimate a high 1:6 ratio between the edge ($= 4 \times d \times t$ where d is the lateral dimension and t is the thickness of the flakes) and surface area ($= 2 \times d^2$) of the WS₂ flakes. We thus suggest that the observed sub-bandgap absorption in the WS₂-SA is also due to the edge-states, promoted by the high edge to surface area ratio of the UALPE WS₂ flakes. This edge-induced sub-bandgap absorption can be saturated at high incident intensities by Pauli blocking, which enables WS₂ to act as an SA material in the near-infrared region. Additionally, a distribution of edge-induced states within the bandgap could explain the wideband saturable absorption experimentally observed here, and in recent reports at a number of different laser wavelengths in other s-TMDs.^{11,12,18–20}

We note that Wang et al. have also proposed a complementary explanation for this phenomenon based on crystallographic defect states, supported by theoretical bandgap studies by varying the ratio of M and S atoms.⁵⁴ Zhang et al.⁵⁵ reported nonlinear optical measurements of WS₂ and MoS₂, grown by high temperature, direct vapor phase sulfurization of pre-deposited metal films. Both materials showed layer dependent saturable and reverse saturable absorption (RSA, due to two-photon absorption) properties. Additionally, the authors demonstrated RSA for 1-3, 18-20, 39-41 layered samples at 1030 nm while SA for 18-20 layers and RSA for 1-3 layer WS₂ at 800 nm. We do not observe any such RSA behavior in our samples (< 8 layers) during the nonlinear measurements (maximum peak intensity, 420 MW/cm²) and Q-switching operation. Another recent report attributes exciton-exciton interaction in bulk and monolayer MoSe₂ (a selenium based s-TMD) for saturable absorption at excitonic resonance.⁵⁶ However, this does not explain the saturable sub-bandgap absorption we observe in our experiments here. A distribution of edge-induced states within the bandgap could better explain the wideband saturable absorption, supported by recent reports on mode-locking or Q-switching at a number of different laser wavelengths in other s-TMDs.^{12,20} We note that grain boundaries and other defects present in s-TMD crystals, such as those grown by CVD may also strongly contribute to such sub-bandgap absorption. Indeed, this may explain ultrafast pulse generation using CVD-grown s-TMDs below the bulk and monolayer bandgap.^{57–60} Considering the above discussion, we propose that the large edge-to-surface ratio of nanoflakes of WS₂, in particular, prepared by UALPE, would be the primary origin of the optical absorption below the fundamental material bandgap. In summary, a free-standing few-layer WS₂-PVA SA has been fabricated by UALPE of chemically pristine WS₂.

Using this SA, we have developed self-starting Q-switched Yb- and Er-doped fiber lasers for short pulse generation. We have proposed edge-induced sub-bandgap states in WS₂ as the primary reason for broadband saturable absorption in the near IR spectral region. This extends our existing understanding for this phenomenon to a wider class of s-TMDs with regard to their potential for future photonic technologies.

References

1. Wang, Q. H., Kalantar-Zadeh, K., Kis, A., Coleman, J. N. & Strano, M. S. Electronics and optoelectronics of two-dimensional transition metal dichalcogenides. *Nat. Nanotech.* **7**, 699–712 (2012).
2. Bonaccorso, F., Sun, Z., Hasan, T. & Ferrari, A. C. Graphene photonics and optoelectronics. *Nat. Photon.* **4**, 611–622 (2010).
3. Hanlon, D. *et al.* Liquid exfoliation of solvent-stabilised black phosphorus: Applications beyond electronics. *arXiv preprint arXiv:1501.01881* (2015).
4. Yun, W. S., Han, S. W., Hong, S. C., Kim, I. G. & Lee, J. D. Thickness and strain effects on electronic structures of transition metal dichalcogenides: 2H-MX₂ semiconductors ($M = \text{Mo, W}$; $X = \text{S, Se, Te}$). *Phys. Rev. B* **85**, 033305 (2012).
5. Hong, X. *et al.* Ultrafast charge transfer in atomically thin MoS₂/WS₂ heterostructures. *Nat. Nanotech.* (2014).
6. Li, D. *et al.* Ultrafast pulse generation with black phosphorus. *arXiv preprint arXiv:1505.00480* (2015).
7. Lu, S. *et al.* Broadband nonlinear optical response in multi-layer black phosphorus: an emerging infrared and mid-infrared optical material. *Opt. Express* **23**, 11183–11194 (2015).
8. Kumar, N. *et al.* Second harmonic microscopy of monolayer MoS₂. *Phys. Rev. B* **87**, 161403 (2013).
9. Wang, R. *et al.* Third-harmonic generation in ultrathin films of MoS₂. *ACS Appl. Mater. Interfaces* **6**, 314–318 (2013).
10. Wang, K. *et al.* Ultrafast saturable absorption of two-dimensional MoS₂ nanosheets. *ACS Nano* **7**, 9260–9267 (2013).
11. Zhang, M. *et al.* Solution processed MoS₂-PVA composite for sub-bandgap mode-locking of a wideband tunable ultrafast Er: fiber laser. *Nano Res.* **8**, 1522–1534 (2015).
12. Woodward, R. *et al.* Few-layer MoS₂ saturable absorbers for short-pulse laser technology: current status and future perspectives [invited]. *Photon. Res.* **3**, A30–A42 (2015).
13. Keller, U. Recent developments in compact ultrafast lasers. *Nature* **424**, 831–838 (2003).
14. Janisch, C. *et al.* Extraordinary second harmonic generation in tungsten disulfide monolayers. *Sci. Rep.* **4** (2014).
15. Hasan, T. *et al.* Nanotube-polymer composites for ultrafast photonics. *Adv. Mater.* **21**, 3874–3899 (2009).
16. Wang, K. *et al.* Broadband ultrafast nonlinear absorption and nonlinear refraction of layered molybdenum dichalcogenide semiconductors. *Nanoscale* **6**, 10530–10535 (2014).
17. Zhou, K.-G. *et al.* Optical materials: Size-dependent nonlinear optical properties of atomically thin transition metal dichalcogenide nanosheets. *Small* **11**, 634–634 (2015).
18. Luo, Z. *et al.* 1-, 1.5-, and 2- μm fiber lasers Q-switched by a broadband few-layer MoS₂ saturable absorber. *J. Lightwave Technol.* **32**, 4077–4084 (2014).
19. Du, J. *et al.* Ytterbium-doped fiber laser passively mode locked by few-layer molybdenum disulfide MoS₂ saturable absorber functioned with evanescent field interaction. *Sci. Rep.* **4** (2014).
20. Woodward, R. *et al.* Wideband saturable absorption in few-layer molybdenum diselenide MoSe₂ for Q-switching Yb-, Er- and Tm-doped fiber lasers. *arXiv preprint arXiv:1503.08003* (2015).
21. Mao, D. *et al.* WS₂ mode-locked ultrafast fiber laser. *Sci. Rep.* **5** (2015).
22. Kassani, S. H. *et al.* All-fiber Er-doped Q-switched laser based on tungsten disulfide saturable absorber. *Opt. Mater. Express* **5**, 373–379 (2015).
23. Wu, K., Zhang, X., Wang, J., Li, X. & Chen, J. WS₂ as a saturable absorber for ultrafast photonic applications of mode-locked and Q-switched lasers. *Opt. Express* **23**, 11453–11461 (2015).
24. Yan, P. *et al.* Microfiber-based WS₂-film saturable absorber for ultra-fast photonics. *Opt. Mater. Express* **5**, 479–489 (2015).
25. Khazaeinezhad, R., Hosseinzadeh Kassani, S., Jeong, H., Yeom, D.-I. & Oh, K. Passively mode-locked fiber laser based on CVD WS₂. In *CLEO: Applications and Technology*, JW2A–74 (Optical Society of America, 2015).

26. Sun, Z., Hasan, T. & Ferrari, A. Ultrafast lasers mode-locked by nanotubes and graphene. *Phys. E* **44**, 1082–1091 (2012).
27. Sun, Z. *et al.* Graphene mode-locked ultrafast laser. *ACS Nano* **4**, 803–810 (2010).
28. Hasan, T. *et al.* Solution-phase exfoliation of graphite for ultrafast photonics. *Phys. Stat. Sol. (b)* **247**, 2953–2957 (2010).
29. Woodward, R. *et al.* Tunable Q-switched fiber laser based on saturable edge-state absorption in few-layer molybdenum disulfide (MoS₂). *Opt. Express* **22**, 31113–31122 (2014).
30. Luo, Z.-C. *et al.* Microfiber-based few-layer black phosphorus saturable absorber for ultra-fast fiber laser. *arXiv preprint arXiv:1505.03035* (2015).
31. Hernandez, Y. *et al.* High-yield production of graphene by liquid-phase exfoliation of graphite. *Nat. Nanotech* **3**, 563–568 (2008).
32. Mason, T. J. & Lorimer, J. P. Applied sonochemistry. *The uses of power ultrasound in chemistry and processing* 1–48 (2002).
33. Coleman, J. N. *et al.* Two-dimensional nanosheets produced by liquid exfoliation of layered materials. *Science* **331**, 568–571 (2011).
34. Coleman, J. N. Liquid-phase exfoliation of nanotubes and graphene. *Adv. Funct. Mater.* **19**, 3680–3695 (2009).
35. Hansen, C. M. *Hansen solubility parameters: a user's handbook* (CRC press, 2007).
36. Cunningham, G. *et al.* Solvent exfoliation of transition metal dichalcogenides: dispersibility of exfoliated nanosheets varies only weakly between compounds. *Acs Nano* **6**, 3468–3480 (2012).
37. Wong, W., Pun, E. & Chan, K. Er³⁺-Yb³⁺ codoped polymeric optical waveguide amplifiers. *Appl. Phys. Lett.* **84**, 176 (2004).
38. Martinez, A. & Sun, Z. Nanotube and graphene saturable absorbers for fibre lasers. *Nat. Photon.* **7**, 842–845 (2013).
39. Butt, H.-J., Graf, K. & Kappl, M. *Physics and Chemistry of Interfaces* (John Wiley & Sons, 2006).
40. Lotya, M. *et al.* Liquid phase production of graphene by exfoliation of graphite in surfactant/water solutions. *J. Am. Chem. Soc.* **131**, 3611–3620 (2009).
41. Smith, R. J. *et al.* Large-scale exfoliation of inorganic layered compounds in aqueous surfactant solutions. *Adv. Mater.* **23**, 3944–3948 (2011).
42. Sugihara, G. *et al.* Thermodynamic study on the Langmuir adsorption of various bile salts including taurine and glycine conjugates onto graphite in water. *Langmuir* **16**, 1825–1833 (2000).
43. Miyajima, K., Machida, K., Taga, T., Komatsu, H. & Nakagaki, M. Correlation between the hydrophobic nature of monosaccharides and cholates, and their hydrophobic indices. *J. Chem. Soc.* **84**, 2537–2544 (1988).
44. Bohren, C. F. & Huffman, D. R. *Absorption and scattering of light by small particles* (John Wiley & Sons, 2008).
45. Beal, A., Knights, J. & Liang, W. Transmission spectra of some transition metal dichalcogenides. II. Group VIA: trigonal prismatic coordination. *J. Phys. C: Sol. State Phys.* **5**, 3540 (1972).
46. Gutiérrez, H. R. *et al.* Extraordinary room-temperature photoluminescence in triangular WS₂ monolayers. *Nano Lett.* **13**, 3447–3454 (2012).
47. Kam, K. & Parkinson, B. Detailed photocurrent spectroscopy of the semiconducting group VIB transition metal dichalcogenides. *J. Phys. Chem.* **86**, 463–467 (1982).
48. Kuc, A., Zibouche, N. & Heine, T. Influence of quantum confinement on the electronic structure of the transition metal sulfide TS₂. *Phys. Rev. B* **83**, 245213 (2011).
49. Roxlo, C., Chianelli, R., Deckman, H., Ruppert, A. & Wong, P. Bulk and surface optical absorption in molybdenum disulfide. *J. Vac. Sci. Technol. A* **5**, 555–557 (1987).
50. Haus, H. A. Theory of mode locking with a fast saturable absorber. *J. Appl. Phys.* **46**, 3049–3058 (1975).
51. Liu, J., Wu, S., Yang, Q.-H. & Wang, P. Stable nanosecond pulse generation from a graphene-based passively Q-switched Yb-doped fiber laser. *Opt. Lett.* **36**, 4008–4010 (2011).
52. Popa, D. *et al.* Graphene Q-switched, tunable fiber laser. *Appl. Phys. Lett.* **98**, 073106 (2011).
53. Degnan, J. J. Optimization of passively Q-switched lasers. *IEEE J. Quantum. Electron.* **31**, 1890–1901 (1995).
54. Wang, S. *et al.* Broadband few-layer MoS₂ saturable absorbers. *Adv. Mater.* **26**, 3538–3544 (2014).

55. Zhang, S. *et al.* Direct observation of degenerate two-photon absorption and its saturation of WS₂ and MoS₂ monolayer and few-layer films. *ACS Nano* (2015).
56. Kumar, N. *et al.* Exciton-exciton annihilation in MoSe₂ monolayers. *Phys. Rev. B* **89**, 125427 (2014).
57. O'Brien, M. *et al.* Transition metal dichalcogenide growth via close proximity precursor supply. *Sci. Rep.* **4** (2014).
58. Zhang, X.-Q., Lin, C.-H., Tseng, Y.-W., Huang, K.-H. & Lee, Y.-H. Synthesis of lateral heterostructures of semiconducting atomic layers. *Nano Lett.* **15**, 410–415 (2014).
59. Lv, R. *et al.* Transition metal dichalcogenides and beyond: Synthesis, properties, and applications of single-and few-layer nanosheets. *Acc. Chem. Res.* **48**, 56–64 (2014).
60. Liu, K.-K. *et al.* Growth of large-area and highly crystalline MoS₂ thin layers on insulating substrates. *Nano Lett.* **12**, 1538–1544 (2012).

Acknowledgements

The authors thank E. J. R. Kelleher for valuable discussions. MZ acknowledges support from Beihang University, China, through a Zhuoyue Bairen Program and TH from the Royal Academy of Engineering through a fellowship (Graphlex).

Author contributions statement

M. Z., L. C. and T. H. conceived the experiments, G. H., G. H., R. C. T. H. conducted the experiments, M. Z., G. H., R. C. T. H. and T. H. analyzed the results, M. Z., L. C., Z. Z. and T. H. wrote the manuscript. All authors reviewed the manuscript.

Additional information

Competing financial interests. The authors declare no competing financial interests.